Towards tsunami early-warning with Distributed Acoustic Sensing: Expected seafloor strains induced by tsunamis

Carlos Becerril[1,2], Anthony Sladen[1], Jean-Paul Ampuero[1,2], Pedro J. Vidal-Moreno[2], Miguel Gonzalez-Herraez[2], Fabian Kutschera[3], Alice-Agnes Gabriel[3,4], and Frederic Bouchette[5]

[1]Université Côte d'Azur, CNRS, Observatoire de la Côte d'Azur, Géoazur Seismology, Valbonne, France
[2]Universidad de Alcalá, Polytechnic School, Department of Electronics, Madrid (Spain)
[3]Scripps Institution of Oceanography, University of California San Diego, La Jolla, CA, USA
[4]Ludwig-Maximilians-Universität München, Munich, Germany
[5]Geosciences-M/GLADYS, Université de Montpellier, CNRS, Montpellier, France

Key Points:

- A review of coupling mechanisms between long-period surface gravity signals (tsunami waves) and seafloor cables.
- Seafloor compliance and the cable's Poisson effect are anticipated to primarily influence DAS responses to tsunami waves.
- Numerical simulations indicate the feasibility of tsunami early-warning via DAS after significant seismic signal filtration.

Corresponding author: Carlos Becerril, carlos.becerril@geoazur.unice.fr

Abstract

Tsunami wave observations far from the coast remain challenging due to the logistics and cost of deploying and operating offshore instrumentation on a long-term basis with sufficient spatial coverage and density. Distributed Acoustic Sensing (DAS) on submarine fiber optic cables now enables real-time seafloor strain observations over distances exceeding 100 km at a relatively low cost. Here, we evaluate the potential contribution of DAS to tsunami warning by assessing theoretically the sensitivity required by a DAS instrument to record tsunami waves. Our analysis includes signals due to two effects induced by the hydrostatic pressure perturbations arising from tsunami waves: the Poisson's effect of the submarine cable and the compliance effect of the seafloor. It also includes the effect of seafloor shear stresses and temperature transients induced by the horizontal fluid flow associated with tsunami waves. The analysis is supported by fully coupled 3-D physics-based simulations of earthquake rupture, seismo-acoustic waves and tsunami wave propagation. The strains from seismo-acoustic waves and static deformation near the earthquake source are orders of magnitude larger than the tsunami strain signal. We illustrate a data processing procedure to discern the tsunami signal. With enhanced low-frequency sensitivity on DAS interrogators (strain sensitivity $\approx 2\times10^{-10}$ at mHz frequencies), we find that, on seafloor cables located above or near the earthquake source area, tsunamis are expected to be observable with a sufficient signal-to-noise ratio within a few minutes of the earthquake onset. These encouraging results pave the way towards faster tsunami warning enabled by seafloor DAS.

Plain Language Summary

Detecting tsunami waves early is crucial to warn people in coastal areas to move to safety. However, monitoring tsunamis far from the coast remain challenging an expensive because it requires a lot of equipment spread out over large areas of the ocean. This research looks into a new method called Distributed Acoustic Sensing (DAS) to detect tsunamis. DAS uses the existing network of undersea fiber optic cables-cables that usually carry internet and telephone signals across oceans. By making slight adjustments to these cables, it is possible to use them to pick up strains in the cable caused by the passing of a tsunami wave. The study shows that by understanding and measuring these strains, DAS can potentially spot tsunamis soon after they start. This method is promising because it uses existing cables, making it a more affordable option for widespread tsunami detection.

1 Introduction

Although several Tsunami Early Warning Systems (TEWS) are in operation worldwide, this is yet to be the norm, mainly due to the high cost associated with the installation and operation of offshore instrumentation with sufficient spatial coverage, density, and real-time data availability. To circumvent these challenges, and as the majority of recorded tsunamis worldwide are directly ascribed to earthquakes (Reid & Mooney, 2023), many TEWS rely on seismic data for source characterization. However, the energy released by the earthquake often is not a sufficient predictor of the tsunami intensity, which may lead to inaccurate early warnings and false alarms (V. Titov et al., 2016; Katsumata et al., 2021). For this reason, the basic sensor package for earthquake and tsunami early warning is a seismometer/accelerometer to detect ground shaking and a pressure gauge to detect tsunami waves (Wilcock et al., 2016). An effective system should use local wave measurements to characterize the tsunami and to allow the detection of tsunamis from other sources such as submarine landslides.

To obtain reliable observations leading to faster tsunami confirmations, it is best to deploy instrumentation directly in the source region, including active subduction zones and areas prone to submarine landslides in volcanic systems. Such observation systems

are crucial for protecting the population and improving our understanding of tsunami generation, which is less understood than the propagation process mainly due to scarce offshore and in-situ observations. The detection of tsunamis in the open ocean, achieved by monitoring variations in water pressure, is significantly challenged by the relatively modest amplitudes of tsunamis — typically around a meter, even for the largest events — and by the logistical complexities and expenses involved in maintaining instruments in remote oceanic locations on a long-term/permanent basis. Additionally, ensuring dense and extensive spatial coverage across all potential tsunami sources complicates this endeavor, making it difficult to rapidly and robustly estimate a tsunami's potential impact. Furthermore, little is known about spatial variations of tsunamis, because too few dense array measurements of tsunamis are available so far (Kohler et al., 2020). As the population grows in coastal regions, the recurrence of tsunami tragedies underscores the urgent need for better detection methods and early warning systems.

Direct tsunami observations are made mostly by coastal tide gauges and fixed moorings or buoys located offshore, such as the Deep-ocean Assessment and Reporting of Tsunamis (DART) system. The current network of 77 DART stations worldwide has a sparse sensor density and a limited spatial footprint. Each DART station consists of a transmitter surface buoy and an anchored seafloor pressure sensor (National Oceanic and Atmospheric Administration (NOAA) Pacific Marine Environmental Laboratory (PMEL) National Center for Tsunami Research (NCTR), 2023). With an approximate cost of US$ 0.5M per station and high maintenance and repair costs, compounded by the remote location of the buoys and required ship operations, densifying DART instrumentation requires a financial commitment which can be prohibitive for developing countries (Bernard & Titov, 2015). Moreover, the DART system is primarily designed for providing forecasts in the case of transoceanic or far-field tsunamis, but not for regional and local tsunamis. A confirmation of tsunami and an evaluation of its amplitude are obtained once the recordings from the closest station are analyzed, which may often take two to three hours (Mungov et al., 2013). Tide gauges are typically located inside harbors and bays, and hence can only have a limited contribution to early warning. Furthermore, the tsunami signal of tide gauge records are often filtered or distorted by the shallow coastal water depth, which makes it difficult to extract detailed information about a tsunami (Saito, 2019).

In rare cases, direct tsunami observations are made by cabled observatories: the North-East Pacific Time-series Undersea Networked Experiments system (NEPTUNE) in Canada (Heidarzadeh & Gusman, 2019), the Dense Oceanfloor Network System for Earthquakes and Tsunamis (DONET) and S-NET systems in Japan. DONET consists of 51 stations over a length of 800 km, whilst S-NET is the world's largest seafloor observation network, consisting of 150 cable-linked seismic and tsunami sensors covering an area of 1000 km x 300 km. Both are deployed on the slopes of subduction zone trenches and in rupture-prone regions, such as those associated with the historical Tonankai and Nankai earthquakes (Aoi et al., 2020). These observation systems have been used to detect several tsunamis of various sizes based on changes in water pressure (Tsushima et al., 2012; V. V. Titov et al., 2005), including the disastrous tsunami of the 2011 Tohoku-oki earthquake (Saito et al., 2011; Maeda et al., 2011). Although capable of carrying robust, long-term observations, cabled observatories require a substantial financial investment, especially to achieve a wide and complete spatial coverage on the scale of subduction zones.

Distributed Acoustic Sensing (DAS) is an emerging technology that re-purposes existing fiber optics in telecommunication cables into long and dense arrays of longitudinal strain sensors (Zhan, 2020). DAS can record external inputs that deform fiber optic cables in a broad frequency range (Paitz et al., 2020), with a current maximum distance range of around 150 km (Waagaard et al., 2021). These capabilities have motivated a decade of applications in subsurface imaging and microseismicity monitoring for energy production and carbon sequestration. DAS arrays have recorded microearthquakes,

regional earthquakes, teleseisms, and infrastructure signals. Analysis of these wavefields is enabling earthquake seismology where traditional sensors were sparse, as well as structural and near-surface seismology. These studies have improved our understanding of DAS instrument response through comparison with traditional seismometers. More recently, DAS has been used to study cryosphere systems, marine geophysics, geodesy, and volcanology (Lindsey & Martin, 2021).

Several key requirements for TEWS are inherent attributes of DAS: low data latency, high spatial density, and relatively low cost, often dominated by the DAS interrogator equipment cost ($\sim$ US$ 150k). Currently commercially available DAS interrogators sense strain with meter-scale spatial resolution over cable spans of up to 150 km and deliver data on land in real-time (Williams et al., 2023; Fernandez-Ruiz et al., 2022; Sladen et al., 2019). Coupling these attributes with the existing (and still expanding) global coverage of the transoceanic telecommunication cable network (Brenne et al., 2024), positions DAS as a sensor package to consider for TEWS. It provides a cost-effective means of deploying instrumentation to monitor offshore locations such as subduction zones, and can also provide several measurements per tsunami wavelength to better study the characteristics of tsunamis.

The earliest reports on seafloor DAS for Earth science documented signals induced by the swell (Sladen et al., 2019; Williams et al., 2019; Lindsey et al., 2019). In particular, (Sladen et al., 2019) showed that the depth-dependence of the signal amplitude is consistent with the pressure depth-dependence from the linear theory of surface gravity waves. This demonstrated that DAS can record surface gravity waves, although at much shorter periods than tsunami waves. The first, and so far only reported detection of a tsunami with seafloor DAS (Xiao et al., 2024) made use of 60 km of cable off the northwestern US coast to detect a far-field tsunami, which produced a small tsunami wave height of $\sim$ 6 mm at a DART station, and reaching $\sim$ 1 cm by the time it reached the end of the monitored fiber. Although the signal-to-noise ratio of the detected tsunami phase was low, even after beamforming, these findings underscore the feasibility of DAS technology to detect tsunami waves.

Several aspects of DAS still need to be addressed to ascertain tsunami wave detection with sufficient signal-to-noise ratio to be integrated into TEWS. DAS is most sensitive to strain along the cable axis. Given that cables are typically laid or buried along the seafloor, they can primarily perform as horizontal arrays of sensors recording horizontal strain, which is not a quantity that has been considered before in tsunami studies. The question of sensitivity at low frequencies also merits attention given that DAS instrumentation usually has lower performance at long periods typical of a tsunami (>100 s) (R. Fernández-Ruiz et al., 2019).

The remainder of the paper is organized as follows. In section 2, we review recently reported developments in the range and sensitivity of DAS at low frequencies, intended to enable improved accuracy over long distances in the mHz frequency range of interest in tsunami studies. They are attained by suppressing the $1/f$ instrument noise, specifically on the chirped-pulse (CP)-DAS architecture that employs linearly chirped laser pulses. Then, to determine the potential contribution of DAS instrumentation in the design of future TEWS, we present a theoretical analysis of the expected seafloor strains potentially induced by tsunami waves. In section 3, we consider two effects arising from the hydrostatic pressure due to the changing sea-surface level: transfer from radial to longitudinal deformation of the cable via Poisson's effect and the deformation of the seafloor via the compliance effect. In sections 4 and 6, we consider the shear strain and temperature changes at the seafloor induced by the lateral water flow associated with tsunami waves. With the aforementioned hydrostatic and shear sources of strain, section 5 simulates the expected strain signal amplitude from a propagating tsunami wave. In section 7, we validate the proposed model by analyzing a 3-D fully coupled simulation of earthquake rupture, seismic, acoustic and tsunami wave propagation.

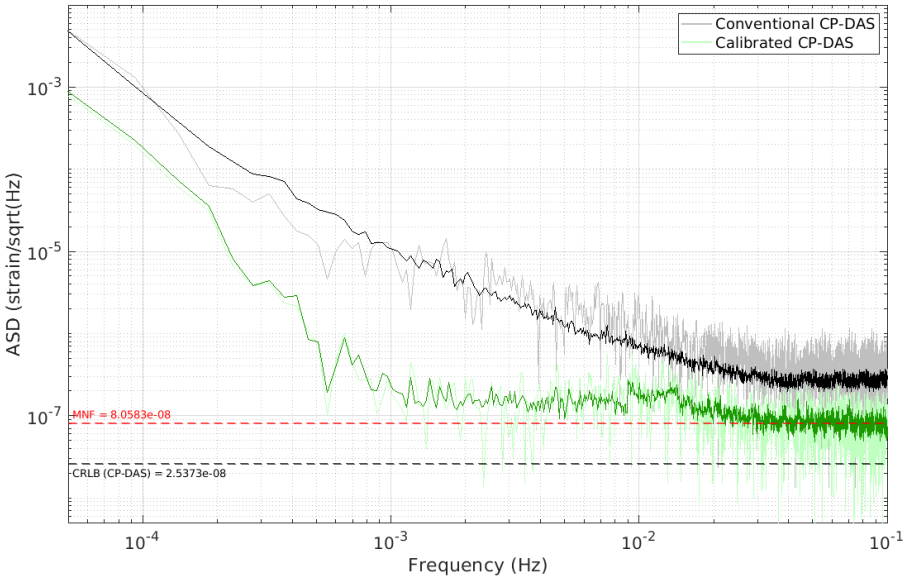

Figure 1. Median Amplitude Spectral Density (ASD) of the noise floor of a conventional chirped-pulse DAS (bold black line) and a DAS unit implementing the multi-frequency database calibration method (bold green line). Light-colored lines are the ASD of an example fiber point (z = 4011 m). The frequency of acquisition was 0.5 Hz. Both conventional and calibrated noise curves only differ in the processing, as it is the same physical measurement, using the same optical traces. The red dashed line is the median noise floor of the bold green line. The black dash line delineates the theoretical noise floor, the Cramer-Rao Lower Bound (CRLB) for this instrument configuration (i.e. frequency of acquisition, chirp bandwidth, signal-to-noise ratio of the optical trace).

2 Sensitivity of Standard and Advanced DAS Instrumentation at Tsunami Frequencies

DAS instrumentation exploits backscattered light from a laser pulse propagating along the optical fiber, due to Rayleigh scattering by inherent heterogeneities along the fiber. Deformation and temperature perturbations to the fiber due to environmental changes cause phase changes in the backscattered light, which are detected via optical interferometry by comparing a measured time-domain trace with a previous fiber reference state. The optical phase recovery methods employed can be complex and add stringent performance requirements on the optical hardware. An advantageous approach is to employ linearly chirped pulses. This allows a frequency-to-time mapping in the backscattered light intensity time-series, which enables direct detection of phase shifts without the need for frequency sweeping or phase unwrapping (Pastor-Graells et al., 2016, 2017). These raw optical measurements are integrated along discrete cable segments, the "gauge length", and then related to position-resolved strain or strain-rate at each "DAS channel".

One of the main limitations of current DAS systems towards applications in tsunami monitoring is their limited sensitivity at low frequencies below 0.01 Hz. Relying on a reference measurement to evaluate the relative phase change of the backscattered light has the drawback that any large strain, temperature fluctuations, or laser frequency noise will cause deviations in the phase shift, potentially rendering the current reference trace

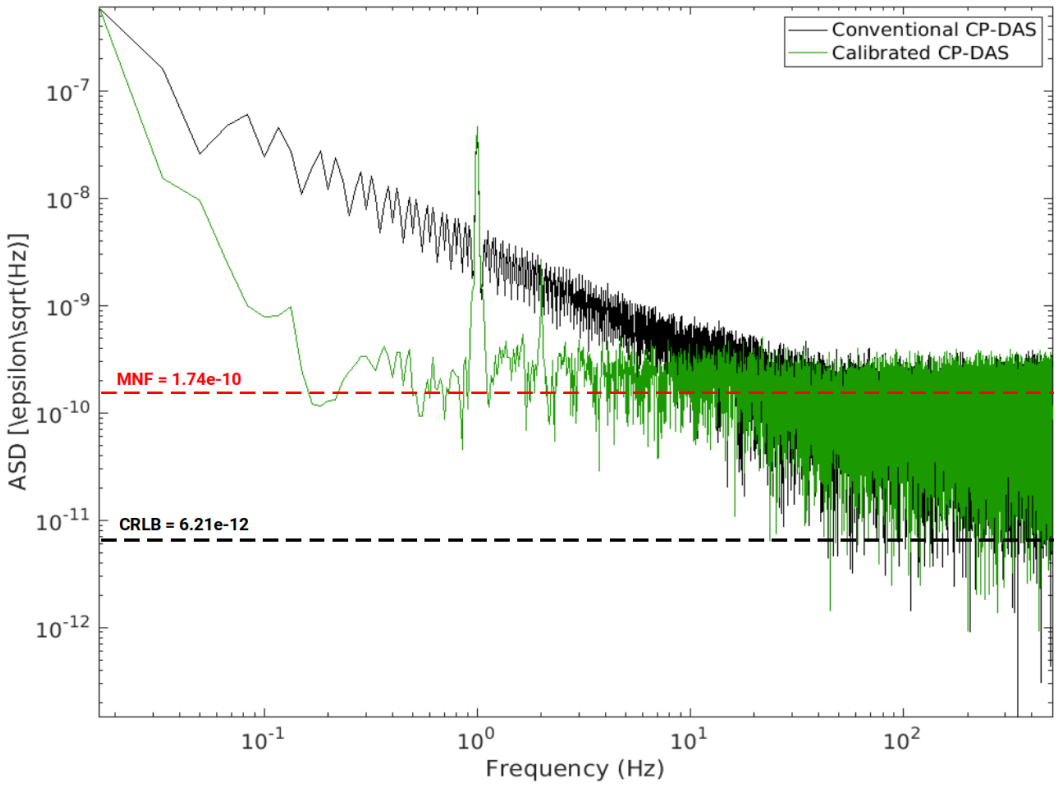

Figure 2. Median Amplitude Spectral Density (ASD) of the noise floor of a conventional chirped-pulse DAS (bold black curve) and a DAS unit implementing the multi-frequency database calibration method (bold green curve). The red dashed line is the median noise floor of the green curve. Further reduction of the noise floor (in comparison to Figure 1), is attained here by improving the stability of the laser and increasing the sampling frequency to 1 kHz. To clearly highlight the benefit of the calibration technique, we introduce a relatively strong 1 Hz modulation of the fiber strain with a piezoelectric transducer (PZT) in order to have regular reference updates in the normal CP-DAS measurement. Due to the high sampling frequency and limitations of our acquisition equipment, we could only resolve frequencies above 15 mHz. During the acquisition, the fiber was in a relatively uncontrolled environment, without temperature drift correction, and we observe an uptake in noise level below $\approx$ 0.2 Hz. The noise floor of the calibrated CP-DAS is flat down to at least 0.1 Hz. This noise floor is expected to extend to lower frequencies if temperature was controlled during acquisition.

invalid. This imposes the need to update such reference, and integrate the short-term variation measurements to obtain absolute strain or temperature variations (Fernandez-Ruiz et al., 2018). However, updating references unavoidably incorporates random noise, which introduces error accumulation over time (noise is integrated with each cumulative variation measurement). This translates into a 1/f noise component, which is detrimental to the determination of very slow processes in the mHz frequency range or below.

The long-term stability of chirped-pulse phase-sensitive optical time-domain reflectometry (CP-ΦOTDR) can be improved with the acquisition of a multi-frequency database to carry out "calibrated" measurements in DAS along an unperturbed fiber (Vidal-Moreno et al., 2022). This approach has been found to suppress reference update-induced 1/f noise,

as the comparison in Figure 1 illustrates. Note that in order to attain sufficient temporal resolution in the sub-mHz regime, and to circumvent limitations in the digital memory of the data acquisition equipment employed in our facilities, the results in Figure 1 have been obtained with a very low acquisition frequency of 0.5 Hz. The DAS noise floor can be decreased further by employing a laser source with an improved wavelength stability, and by increasing the frequency of acquisition. For fiber lengths up to 100 km, the acquisition frequency can be raised to 1 kHz, resulting in a mean noise floor of $\epsilon \approx 2\times 10^{-10}$ as exemplified in Figure 2. Due to the relatively high acquisition trigger frequency, and the aforementioned limitations in the data acquisition equipment, we are only able to probe the fiber for about 1 minute, allowing to resolve frequencies above 15 mHz. Furthermore, the steady climb in noise levels at the low frequencies in both Figures 1 and 2 is due to the relatively uncontrolled environment; no temperature control was implemented to mitigate in-lab temperature fluctuations, hence this is most likely temperature drift. Despite these limitations, these acquisitions show a considerable improvement in canceling instrument-generated 1/f noise. Without temperature drifts, the noise floor limit obtained here at high frequencies likely extends to lower frequencies, and is perhaps limited by the temperature fluctuations inherent to ocean-bottom environments.

Unlike phase-based DAS (ΦOTDR) which relies on retrieving the phase of backscattered light limited to values between $-\pi$ and π (Masoudi et al., 2013; Diaz-Meza et al., 2023); with the chirped-pulse architecture (CP-ΦOTDR), the measurable dynamic range is limited in the maximum strain variation between pulse and reference, $\Delta\epsilon_{max}$, which induces a temporal shift, such that it renders the reference measurement inaccurate (Bhatta et al., 2019). This is a function of the spectral characteristics of the chirped pulse (R. Fernández-Ruiz et al., 2019). With the configuration illustrated in Figure 2, for the conventional chirped-pulse DAS (5 GHz chirp content at 1 kHz acquisition rate) this corresponds to $\Delta\epsilon_{max} \sim \pm 10^{-6}$ before the instrument resorts to updating the reference (and accumulating 1/f noise). For the calibrated version of the instrument this limit becomes $\pm 82.5\times 10^{-6}$ (Vidal-Moreno et al., 2022).

In the following sections, we adopt as reference DAS sensitivity at all relevant frequencies the improved mean noise floor shown in Figure 2, $\epsilon \approx 2 \times 10^{-10}$.

3 Strain of Seafloor Optical Fibers from Water Pressure Loading

Here, we estimate the expected amplitude of seafloor horizontal strains that could be generated by the hydrostatic pressure variations induced by the changes in water height via two effects: the compliance effect of the seafloor and the Poisson's effect of the cable.

3.1 Compliance Effect

The water pressure perturbation induced by a tsunami wave acts on the seafloor and deforms it elastically. The problem of determining the strain of an elastic half-space caused by a normal force on its surface was first considered by J. V. Boussinesq. In this formulation, the solid Earth is approximated by a homogeneous, isotropic, linear elastic half-space. Neglecting the spherical geometry of Earth is adequate because we consider tsunami wavelengths that are short compared to Earth's radius. Details of the solution are given by (Steketee, 1958), from which we take the expression for horizontal displacement parallel to the cable axis ($\bar{u}_x$) in the wavenumber domain (spatial Fourier transform):

$$\bar{u}_x = ik_x \frac{\bar{P}}{2\mu k^2}\left(1 - \frac{1}{\alpha} + kz\right)e^{-kz} \tag{1}$$

where z is the vertical coordinate, defined as pointing upwards,

$$\alpha = \frac{\lambda + \mu}{\lambda + 2\mu}, \tag{2}$$

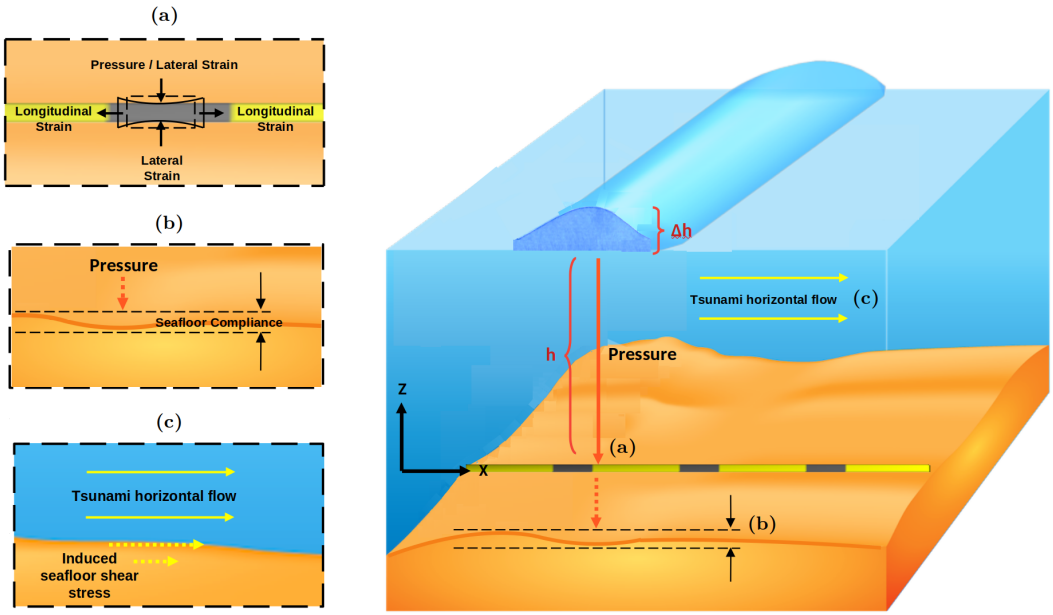

Figure 3. Illustration of a submarine cable in the presence of a propagating tsunami wave. Vertical pressure loading due to changes in the water column, Δh give rise to **(a)** longitudinal elongation of the cable due to the Poisson effect and **(b)** deformation of the seafloor (compliance). The horizontal flow motion beneath the tsunami wave induces **(c)** shear stress on the seafloor surface. Also shown is the coordinate system convention and definition of relevant variables.

λ and μ are Lamé's elastic moduli, and $k = \sqrt{k_x^2 + k_y^2}$ is the amplitude of the wavenumber vector (k_x, k_y) along the horizontal plane. The horizontal displacement at the seafloor $(z = 0)$ is

$$\bar{u}_x = ik_x \frac{\bar{P}}{2\mu k^2}\left(1 - \frac{1}{\alpha}\right) \quad = -ik_x \frac{\bar{P}}{2k^2(\lambda + \mu)} \tag{3}$$

The strain along the cable axis (x-axis), which is the quantity measured by DAS, is $\epsilon_x = \frac{du_x}{dx}$. Since its Fourier transform is $\bar{\epsilon}_x = ik_x\bar{u}_x$, we obtain:

$$\bar{\epsilon}_x = \frac{k_x^2}{k^2}\frac{\bar{P}}{2(\lambda + \mu)} \tag{4}$$

Defining θ as the angle between the wavenumber vector (the tsunami wave propagation direction) and the cable axis, we have $k_x/k = \cos\theta$ and $\bar{\epsilon}_x = \frac{\bar{P}\cos^2\theta}{2(\lambda+\mu)}$. Taking the inverse Fourier transform of $\bar{\epsilon}_x$, the amplitude of seafloor strain oscillation induced by a single tsunami plane wave is

$$\epsilon_x = \frac{P\cos^2\theta}{2(\lambda + \mu)} \tag{5}$$

We obtain a generic estimate of the amplitude of this effect by taking the average over all possible tsunami wave directions:

$$\epsilon_{xavg} = \frac{P}{4(\lambda + \mu)} \tag{6}$$

3.2 Poisson's Effect

Another potential contribution to the strain signal detected by DAS is from Poisson's effect: water pressure perturbations cause radial compression of the submarine cable, which in turn induces longitudinal elongation of the cable through Poisson's effect. We assume that water pressure acts isotropically on the whole circumference of the cable, neglecting the fact that the cable might be partially buried. Representing the cable as an effective homogeneous medium with effective Young's modulus E and Poisson's ratio ν, its longitudinal strain due to Poisson's effect is given by (Tatekura et al., 1982):

$$\epsilon_x = 2\frac{1-2\nu}{E}P \tag{7}$$

The cable's sensitivity to pressure is highly dependent on the cable design. For an optical submarine cable assembly, $E \sim 5-50$ GPa and $\nu \sim 0.2-0.25$ (Kojima et al., 1982; Tatekura et al., 1982). The lower values of E and larger values of ν correspond to less armored cables. For a submarine cable with mid-range elastic properties ($\nu = 0.23$ and $E = 25$ GPa) the Poisson's effect sensitivity is $\epsilon_x \sim 4.3 \times 10^{-11}\ \Delta P$, which falls within expectations based on previously reported theoretical estimates (Budiansky et al., 1979; Haavik, 2022).

3.3 Expected Strain Signal from Hydrostatic Pressure

Here we combine the two pressure effects and estimate their total expected contribution to seafloor DAS strain as a function of tsunami wave height and frequency. We stay within the linear regime of the tsunami theory. This framework assumes that the wave amplitude (typically less than 10 meters) is much smaller than the wavelength. This assumption is generally violated only during the final stage of wave breaking near the coast, or under extreme tsunami generating conditions. We neglect the feedback of seafloor compliance on tsunami waves, which is significant at much longer periods and propagation distances than considered here (Tsai et al., 2013); we thus adopt the conventional tsunami theory with a rigid seafloor. We assume an incompressible, homogeneous, and non-viscous ocean, subject to a constant gravitational field, with uniform water depth h.

Within this framework, the frequency ω and wavenumber k of a sea surface gravity wave satisfy the dispersion relation (Watada, 2013)

$$\omega^2 = gk\tanh(kh) \tag{8}$$

where g is the gravitational acceleration. For a given frequency within the range of interest in tsunami studies, and for sea depths h ranging from 500 meters to 6 km, we solve the above relation for the corresponding kh. The amplitude of the pressure induced by a sea surface height anomaly (SSHA) of amplitude Δh, at a vertical position z relative to the seafloor, is

$$P(z) = \rho g \Delta h \frac{\cosh(kz)}{\cosh(kh)} \tag{9}$$

The seafloor pressure amplitude (at $z = 0$) is thus

$$P = \frac{\rho g \Delta h}{\cosh(kh)} \tag{10}$$

The cosh term induces a low-pass filter effect: only long wavelengths generate significant seafloor pressure changes. As a validaton of this linear theory of surface gravity waves with DAS data, (Sladen et al., 2019) showed that the depth-dependence in equation 10 is consistent with the decay with depth of the amplitude of DAS signals from swell.

We calculate seafloor pressure for values of Δh (SSHA) of 0.1 and 1 meter representative of intermediate and large-size tsunamis in the open ocean. We use the resulting pressure to calculate the longitudinal cable strain due to the compliance effect and

Poisson's effect through Equations (5) and (7), respectively. We add the two effects to obtain the total DAS strain due to pressure perturbations. To evaluate the compliance effect, for a given frequency, we consider elastic parameters λ and μ from the Preliminary Reference Earth Model (PREM) (Dziewonski & Anderson, 1981) averaged down to a depth proportional to the tsunami wavelength, namely $1/k$ (Crawford, 2004). For wavelengths between 10 and 100 km, Equation 5 yields a sensitivity to pressure via the compliance effect of $\epsilon_x \sim (5.5 \times 10^{-11} - 4.8 \times 10^{-12})\ \Delta P$.

With the elasticity parameters considered in this study for the cable assembly and those from the PREM model, the sensitivity to Poisson's (estimated in the previous section) and compliance effects are very similar. One feature that might help distinguish their relative contributions in field data is that only the compliance effect depends on the wave propagation direction (θ is involved in Equation (5) but not in Equation (7)).

The sum of Poisson's and compliance effects yields an order-of-magnitude theoretical estimate of pressure sensitivity of $\epsilon_x/\Delta P \sim 10^{-10}$ Pa^{-1}. This is similar to or somewhat smaller to the observations made by Meulé et al. (2024), and recent empirical estimates: $\epsilon_x/\Delta P \sim 5 \times 10^{-10}$ Pa^{-1} in (Williams et al., 2023), $\epsilon_x/\Delta P \sim 10^{-9}$ Pa^{-1} in (Glover et al., 2024). The latter estimate was obtained in shallow water ($\leq$15 m) and for relatively short wavelengths associated to frequencies in the 0.04-0.3 Hz band, thus the difference can be partly attributed to the lower stiffness of shallow sediments and to larger contributions from shoaling and seafloor shear effects. An additional order-of-magnitude verification is based on DAS signal amplitudes reported by (Sladen et al., 2019) for surface gravity waves recorded at shallow depths ($<$ 100 m). Considering their observed strain rates (extrapolated) at zero depth $\dot{\epsilon} \sim 2 \times 10^{-7}$ s^{-1}, their dominant period $\sim$ 10 s, and $\epsilon_x/\Delta P \sim 10^{-10}$ Pa^{-1}, yields $\Delta P \sim 10^4$ Pa. This pressure corresponds to $\Delta h \sim$ 1 m, which agrees in order-of-magnitude with reported wave heights in the same region (Guerin et al., 2022).

Figure 4a,b shows the resulting strains as a function of frequency, along with the mean noise floor illustrated in Figure 2 for the calibrated version of a chirped-pulse DAS instrument. The strain amplitudes yield signal-to-noise ratios (SNR) larger than 100 for a wave height of 0.1 m, and SNR $>$ 1000 for a wave height of 1 m. These results suggest that DAS could reliably detect signals from the pressure induced by tsunami waves. The stacking of multiple DAS channels could further improve detectability; with typical DAS gauge lengths $\sim$ 10 m, it would be feasible to stack 100 channels along cable segments of $\sim$ 1 km length that are still much shorter than a typical tsunami wavelength, potentially improving SNR by a factor of 10.

4 Seafloor Strain from Shear Stress Beneath a Tsunami Wave

The displacement of water masses by a tsunami wave can induce sea-bottom shear strain. The horizontal free-stream velocity beneath a tsunami wave of frequency ω can be estimated from the particle velocities given by linear wave theory (Dean & Dalrymple, 1991):

$$v_x(x,t) = A\frac{\cosh(kz)}{\sinh(kh)}\sin(kx-\omega t)$$
$$v_z(x,t) = A\frac{\sinh(kz)}{\sinh(kh)}\cos(kx-\omega t) \quad (11)$$

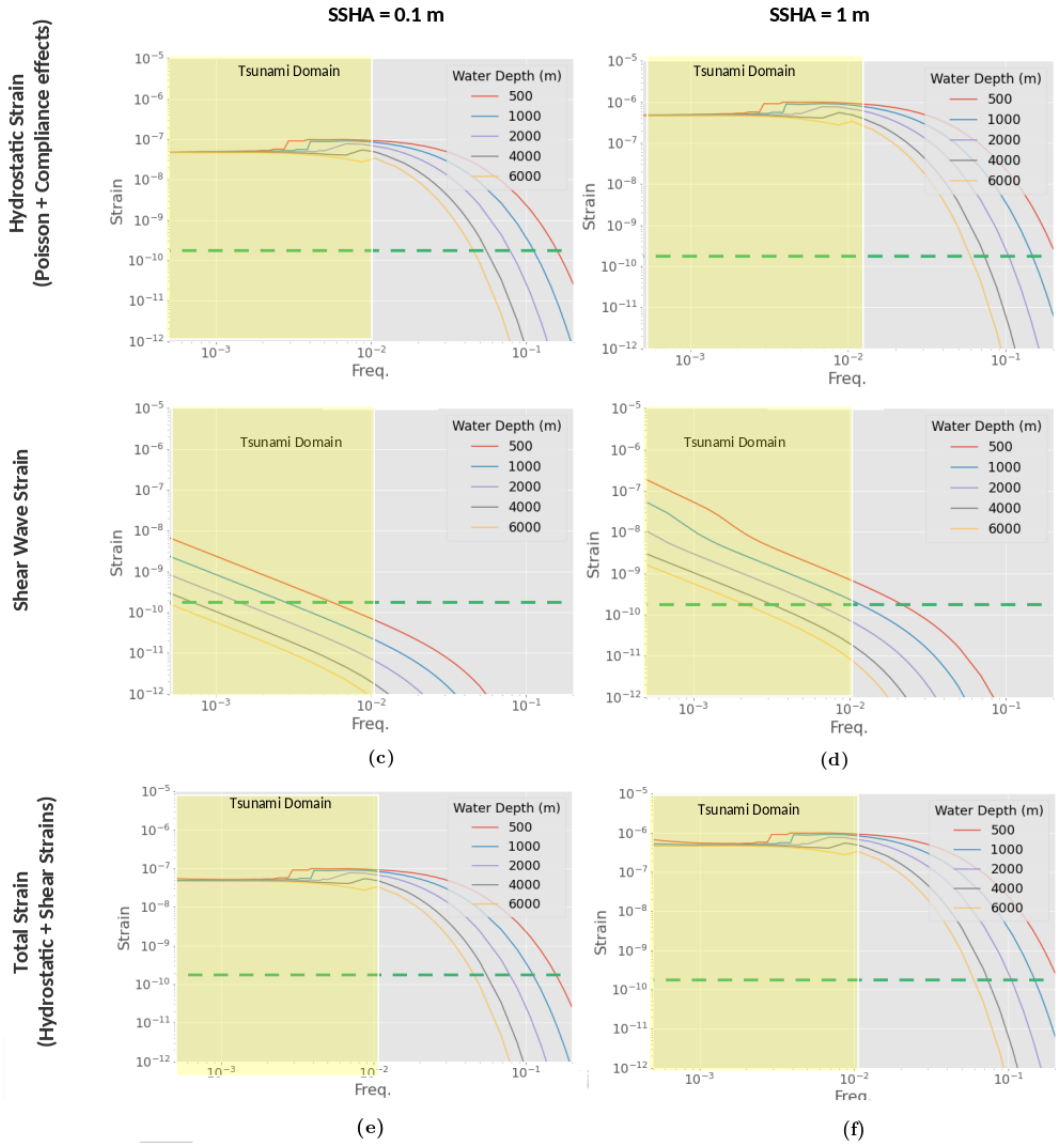

Figure 4. Expected strain amplitudes for tsunami heights (sea surface height anomalies, SSHA) of 0.1 m and 1 m, as indicated in the column headers. Figures in rows correspond to the strain from hydrostatic pressure at the seafloor (a-b), the bottom strain due to the shear stress from the horizontal flow motion beneath a tsunami wave (c-d), and the combined strain from the aforementioned sources of strain (e-f). The different colored curves represent different sea depths h as indicated on each legend; the green dashed line represents the noise floor for the calibrated DAS unit. The yellow-shaded region encompasses the range of frequencies corresponding to tsunami waves. For the cable assembly, nominal values of E=25 GPa and ν=0.23 were used for Young's modulus and the Poisson's ratio, respectively. The seafloor is modeled as a stratified solid with elastic properties based on the PREM model. The ocean has a density ρ = 1030 kg/m3, the ocean has an acoustic wave speed of c_p = 1500 m/s and the water particle viscosity ν_s = 1E-6 m2/s.

where v_x and v_z are the horizontal and vertical particle velocities, respectively, z is vertical position relative to the seafloor, and

$$A = \frac{\Delta h}{2}\sqrt{\frac{g}{h}} \tag{12}$$

The vertical velocity peaks at the ocean surface and decays exponentially to zero at the seafloor. In contrast, the horizontal velocity remains relatively constant through the water column.

At the seafloor ($z = 0$):

$$v_x(x,t) = \frac{\Delta h}{2}\sqrt{\frac{g}{h}}\frac{1}{\sinh(kh)}\sin\left(kx - \omega t\right) \tag{13}$$

The resulting bottom shear stress is

$$\tau_w = \frac{\rho}{2} f v_x^2 \tag{14}$$

where f is the friction coefficient. The associated shear strain is

$$\epsilon_{shear} = \frac{\tau_w}{\mu} \tag{15}$$

where μ is the elastic shear modulus of the seafloor.

The friction coefficient that should be used under a tsunami wave is determined by the flow regime on the bottom boundary layer. According to the analysis by (Tinh & Tanaka, 2019), for most of the propagation phase, the tsunami-induced bottom boundary layer shows an unsteady behavior and resembles that induced by wind-driven waves, even under long-period wave motion; with the transition from wave to steady-motion typically occurring only a few meters from shore. The bottom boundary layer at the tsunami source is within the laminar regime and subsequently, a transition occurs to smooth turbulence during the shoaling process, with a transition from smooth to rough turbulent region at shallow depths. In this study, the full-range equation proposed by (Tanaka et al., 2020, Eq.18) for the wave–current combined motion, is implemented to compute the wave friction coefficient under shoaling tsunami, f_w, given that it yields a smoothly interpolated value for each of the aforementioned flow regimes including the transitional domain. The full-range equation is a function of the wave-induced velocity v_x, the angular frequency of the wave, ω, the roughness of the seabed material (sand grain diameter), and the viscosity of the fluid.

Figure 4c,d shows the estimated shear strain levels as a function of frequency. Figure 4e,f summarises the total expected strain signal at the seafloor from Poisson's effect, seafloor compliance, and bottom shear strain. The two first effects are largely dominant. The shear strain has an appreciable impact only at low frequencies, at shallow depth, and high SSHA (the case $h = 500$ m and $\Delta h = 1$ m in Figure 4f).

5 Strain from a Propagating Tsunami Wave

To study the strain signal as a tsunami wave propagates, we consider a tsunami wave traveling from its source towards the coast, up to a water depth of $h = 100$ m. In the source area, the wave height is Δh_0 and the water depth is h_0. To estimate the evolution of strain during the shoaling process, we approximate the spatial variation of wave height Δh using Green's law:

$$\Delta h = \Delta h_0 \left(\frac{h_0}{h}\right)^{1/4} \tag{16}$$

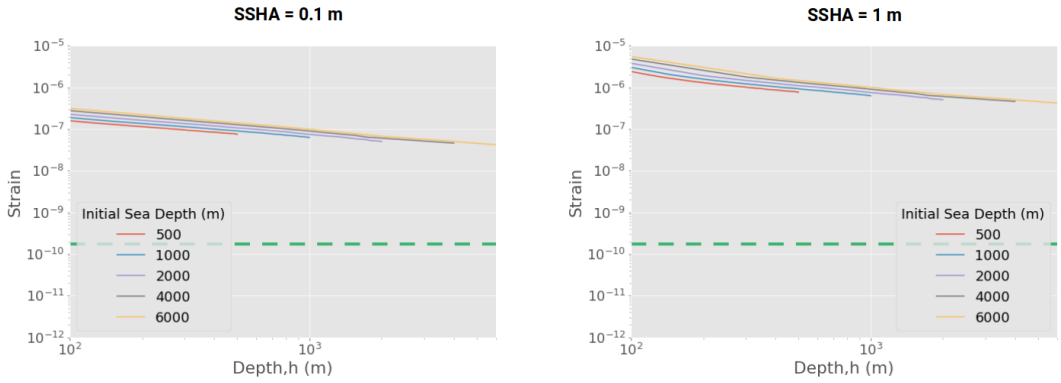

Figure 5. Calculated strain amplitudes from traveling tsunami waves generated at various sea depths h (indicated on the legend) and propagating through decreasing water depths towards the coast, up to a depth of 100 m. Results are for initial tsunami heights - sea surface height anomalies (SSHA) of (a) 0.1 m and (b) 1 m. These results are the average from 0.5 mHz to 11 mHz, and represent the total combined strain from hydrostatic seafloor pressure and the bottom shear stress due to the horizontal flow motion beneath a tsunami wave. The green dashed line represents the noise floor of the calibrated DAS unit.

For each water depth value h, the corresponding wave height Δh is calculated. These values are then used to calculate the wavenumber k through equation (8), for a range of frequencies between 0.5 mHz up to 11 mHz. This is then used to compute the total strain resulting from the three effects considered so far.

Once again, we observe that the strain from hydrostatic pressure is the dominant signal for most of the tsunami trajectory. The contribution from shear strain becomes appreciable only for the cases with initial SSHA = 1 m (Figure 5b), when the tsunami wave reaches shallower depths. This manifests as a slight increase of the slope of each curve at shallow depths in comparison to Figure 5a.

The tsunami strain signal yields an SNR of at least 200, reaffirming the feasibility of tsunami wave detection with DAS instrumentation. Towards implementation, in the following sections, we consider signals that may overlap with tsunami signals, potentially affecting detection capabilities.

6 Influence of Temperature Perturbations

Temperature and strain signals co-exist in DAS data. Both phenomena affect the optical path along a fiber: strain perturbations change the fiber length and temperature fluctuations change the refraction index through the thermo-optical effect. Temperature perturbations ΔT produce a proportional apparent DAS strain perturbation $\Delta\epsilon$. The proportionality factor is a function of the refractive index, thermo-optic and elasto-optic responses of the fiber silica (Fernandez-Ruiz et al., 2022; Haavik, 2022; Hartog et al., 1979). A representative estimate is:

$$\Delta\epsilon \approx 10^{-5} \times \Delta T \tag{17}$$

The mean noise floor $\epsilon \approx 2 \times 10^{-10}$ of the DAS instrument under consideration corresponds to a temperature perturbation of approximately 20 μK. Given such fine sensitivity, it is necessary to evaluate whether thermal effects may overlap with the mechanical strain signals induced by tsunami waves. Here we consider thermal effects due to (1) background temperature fluctuations and (2) tsunami-induced fluid advection.

6.1 Background Temperature Fluctuations

Long-term oceanographic observations in deep water indicate that temperature fluctuations at the ocean bottoms generally have dominant periods ranging from hours to weeks. Their frequency content is highly dependent on site characteristics (depth, geographic location, bathymetry, etc). For our purposes, such long-period signals can be filtered out if they do not overlap with the tsunami period range.

Frequency content and water depth can serve as a basis to distinguish strain from temperature signals in DAS seafloor data. At shallow water depths (< 200 m) and at short periods (10^{-2} – 10^{2}s), mechanical strains from seismic, acoustic or surface gravity waves dominate over thermal fluctuations driven by the oceanic environment. This differentiation has allowed seismic phase detection with ocean-bottom DAS (e.g., Lior et al. (2020); Ugalde et al. (2022)) and observations of coastal currents (Lindsey et al., 2019; Williams et al., 2019). In deep water or at long periods, thermal and mechanical DAS signals may have comparable amplitudes.

Recent studies suggest ocean-bottom DAS can record temperature. (Ide et al., 2021) interpreted DAS signals at tidal periods and with apparent propagation speeds of 0.5 m/s, recorded along a cable offshore Japan, as temperature fluctuations of a few Kelvins due to water advection driven by tides. (Williams et al., 2023) observed, along a cable off the island of Gran Canaria, the propagation of thermal fronts associated with nonlinear internal tides, with apparent velocities in the 0.1 - 0.5 m/s range.

In general, thermal anomalies driven by oceanographic processes are larger in shallow waters. Ocean-bottom DAS data confirms that temperature fluctuations are weaker with increasing depth. Off the coast of Toulon, France, (Pelaez Quiñones et al., 2023) found temperature fluctuations in the 0.1 - 1 mHz band reaching 0.1 K at depths shallower than 100 m and about 0.01 K at further depths down to 2000 m, with apparent velocities close to 0.1 and 0.01 m/s, respectively. Off Gran Canaria, (Williams et al., 2023) observed perturbations up to about 2 K at 1.4 km depth and 0.2 K at 2.5 km depth.

The thermal DAS signals due to internal waves and tides may overlap with the mechanical DAS signals due to tsunami waves in the mHz range. From (17), fluctuations larger than 0.01 K will correspond to strain signals above 10^{-7}, which may exceed tsunami signal amplitudes (Figure 4e,f). Yet, these temperature anomalies propagate about 3 orders of magnitude slower than tsunami waves, thus it should be possible to filter them out based on their apparent speed $C_x = C/\cos(\theta)$, where C is the phase velocity and θ is the angle between the direction of propagation of the temperature front and the cable orientation. Although oblique incidence tends to increase the apparent velocity, only a very narrow range of incidence angles, within 0.2° from normal incidence, would make the temperature signal velocity comparable to tsunami velocities. Hence, frequency-wavenumber filtering based on signal speed is expected to be a viable approach.

If the cable is not straight, the wavenumber decomposition cannot be obtained by Fourier transform, and alternate strategies need to be devised. This may consist of in situ calibration of the instrument by characterizing temperature variations that may be pervasive and endemic to a given offshore location; to consider cable construction and burial, and to make key observations of the environment. Temperature fluctuations on seafloor DAS recordings may also be mitigated by burying the cable. Indeed, (Pelaez Quiñones et al., 2023) and (Williams et al., 2023) reported a lack of temperature signals along cable sections that are buried. While buried sections along telecom cables are rare, they could be a design consideration for fiber optic cables tailored for geophysical monitoring.

6.2 Tsunami-Induced Temperature Fluctuations

In principle, seafloor temperature perturbations can arise from advection of the thermally stratified water column by a tsunami wave. However, such signals have not been observed yet. Temperature data during tsunamis has been fortuitously recorded in association with seafloor pressure observations, as part of the system that compensates for the thermal drift of pressure transducers (Eble et al., 1989; Joseph, 2011). One ocean bottom station in the 2011 M_w=9.0 Tohoku earthquake source area, at a sea depth of 1.1 km, recorded a water temperature increase of 0.19 °C about 3 h after the earthquake, lasting for several hours (Inazu et al., 2023). This temperature transient was attributed to a tsunami-generated turbidity current (Arai et al., 2013). During the 2003 M_w=8.3 Tokachi-oki earthquake and tsunami, a CTD (Conductivity-Temperature-Depth) station located in the source area recorded a temperature perturbation at least two hours after the mainshock, which was attributed to a benthic storm (Mikada et al., 2006). Furthermore, the temperature data at two seafloor pressure stations found no significant change in the tsunami pressure signal after applying a temperature correction (Inazu & Hino, 2011). As the temperature measurements from quartz crystal transducers are primarily intended to compensate for the thermal drift of the pressure gauge, their temperature resolution is limited. In the absence of well-resolved observations of tsunami-induced seafloor temperature changes, we turn next to back-of-the-envelope theoretical analysis.

An order-of-magnitude estimate shows that temperature changes due to deep water advection by a tsunami wave could be recorded by seafloor DAS, but would be much smaller than the strain mechanically induced by the tsunami. Considering a SSHA of 10 cm, the horizontal water particle displacement at the sea bottom is of at least 1 m (Ward, 2003). Assuming this same horizontal advection follows along a typical slope of 5% between a continental shelf and a subduction trench, it displaces water vertically by 0.05 m along the slope. Considering a generic vertical temperature gradient for the open ocean of 0.002 K/m at depths exceeding 1 km (Talley, 2011), the vertical water advection carries a temperature change of $\sim$ 0.1 mK. This value corresponds to a DAS strain $\sim 10^{-9}$, which is above the calibrated DAS noise floor of 2×10^{-10}, but about two orders of magnitude below the expected strain mechanically induced by tsunami waves (Figure 4e).

7 Comparison to Fully Coupled Earthquake and Tsunami Simulations

With the improvements to DAS instrument sensitivity at low frequencies illustrated in Figure 2, our analysis of the expected seafloor strain due to tsunami waves (Figures 4 and 5) points to the feasibility of tsunami detection with seafloor DAS. To further demonstrate the potential contribution of DAS to TEWS, we analyze here a synthetic data set from a fully physics-based 3D simulation of earthquake dynamic rupture and tsunami generation.

7.1 Coupled Ocean-solid Earth Simulation Setup

We consider an idealized megathrust earthquake on a low-angle planar thrust fault, with subsequent tsunami generation and propagation across a compressible ocean layer with constant depth. The model setting is based on a benchmark scenario for linking earthquake and tsunami simulations established in (Madden et al., 2021; Krenz et al., 2021). The fault strikes North, is 200 km wide along the strike, extends from the surface to 35 km depth, and dips eastward with a 16° dip angle (Figure 6). The ocean has a water depth of 2 km, acoustic wave speed of c_p = 1500 m/s and density ρ = 1000 kg/m^3. The solid half-space has homogeneous elastic properties representative of oceanic crust: P-wave speed c_p = 7639.9 m/s, shear wave speed c_s = 4229.4 m/s and density ρ = 3775 kg/m^3.

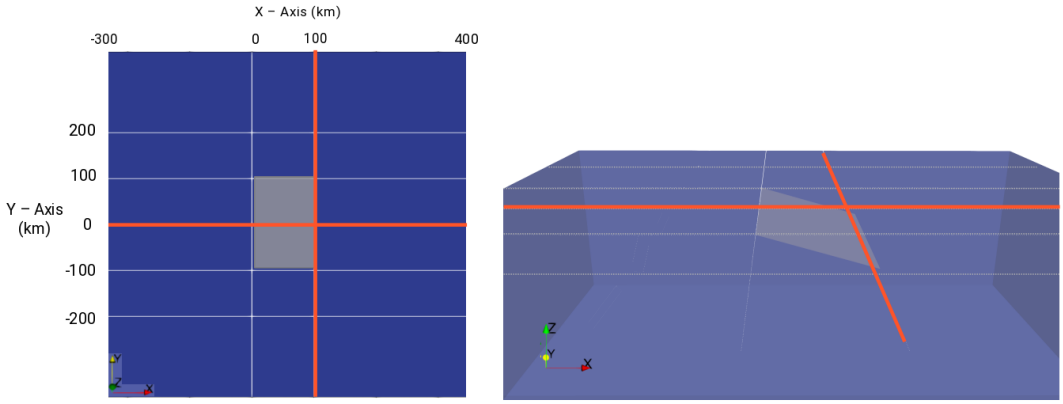

Figure 6. Benchmark simulation scenario showing location and dimensions of the planar subducting plate relative to the receiver matrix. The simulation space encompasses an area of approximately 750 km × 750 km, with a uniform 2 km water layer atop. Receivers along each linear array are arranged in pairs separated by 50 m, respectively, which emulates commonly used DAS gauge lengths; the next adjacent receiver pair is placed 450 m apart. The simulation consisted of two identical matrices, one buried 10 cm below the seafloor, whilst the other matrix is located 10 cm below the sea surface. Given the orientation of the subducting plate, increasing positive values move towards the coast along the X-axis, whilst negative values go seaward. X and Y coordinate values are given in meters. The highlighted arrays at Y = 0 km and X = 100 km are used in this analysis.

Because this setup ignores the presence of shallow compliant layers, the resulting seafloor compliance signal should be understood as a lower bound.

The simulation employs a fully coupled 3-D earth and ocean model of earthquake dynamic rupture, seismic and acoustic wave propagation, whilst simultaneously solving for the tsunami (gravity) wave propagation, implemented in the simulation package SeisSol (www.seissol.org). The tsunami is modeled through linearized equations, derived by combining mass balance with a linearized equation of state and momentum balance, with gravity acting as a restoring force and an initial small perturbation about the hydrostatic rest state of the ocean (Lotto & Dunham, 2015). The simulation self-consistently computes the full wavefield in 3-D, which comprises seismic, acoustic, and surface gravity waves in elastic (earth) and acoustic (ocean) media.

SeisSol is based on the arbitrary high-order derivative Discontinuous Galerkin (ADER-DG) method and optimized for modern high-performance computing infrastructure (e.g., Heinecke et al. (2014); Uphoff et al. (2017); Krenz et al. (2021)). Here, we use a fifth-order accurate scheme and an unstructured tetrahedral mesh with a minimum element size of 66 m (on the fault), consisting of 29.5 million elements. We simulate 10 minutes of combined earthquake dynamic rupture, tsunami generation, and tsunami propagation on the supercomputer SuperMUC-NG, which requires a total of ∼460,000 CPUh using 512 nodes (24,576 cores) for ∼18.7 hours.

The earthquake source evolves spontaneously during the earthquake dynamic rupture simulation governed by linear slip-weakening friction (e.g., Harris et al. (2018)). The earthquake hypocenter is located in the southeast corner of the fault at 26 km depth. While the fault does reach the seafloor, the rupture itself is buried; higher fault strength

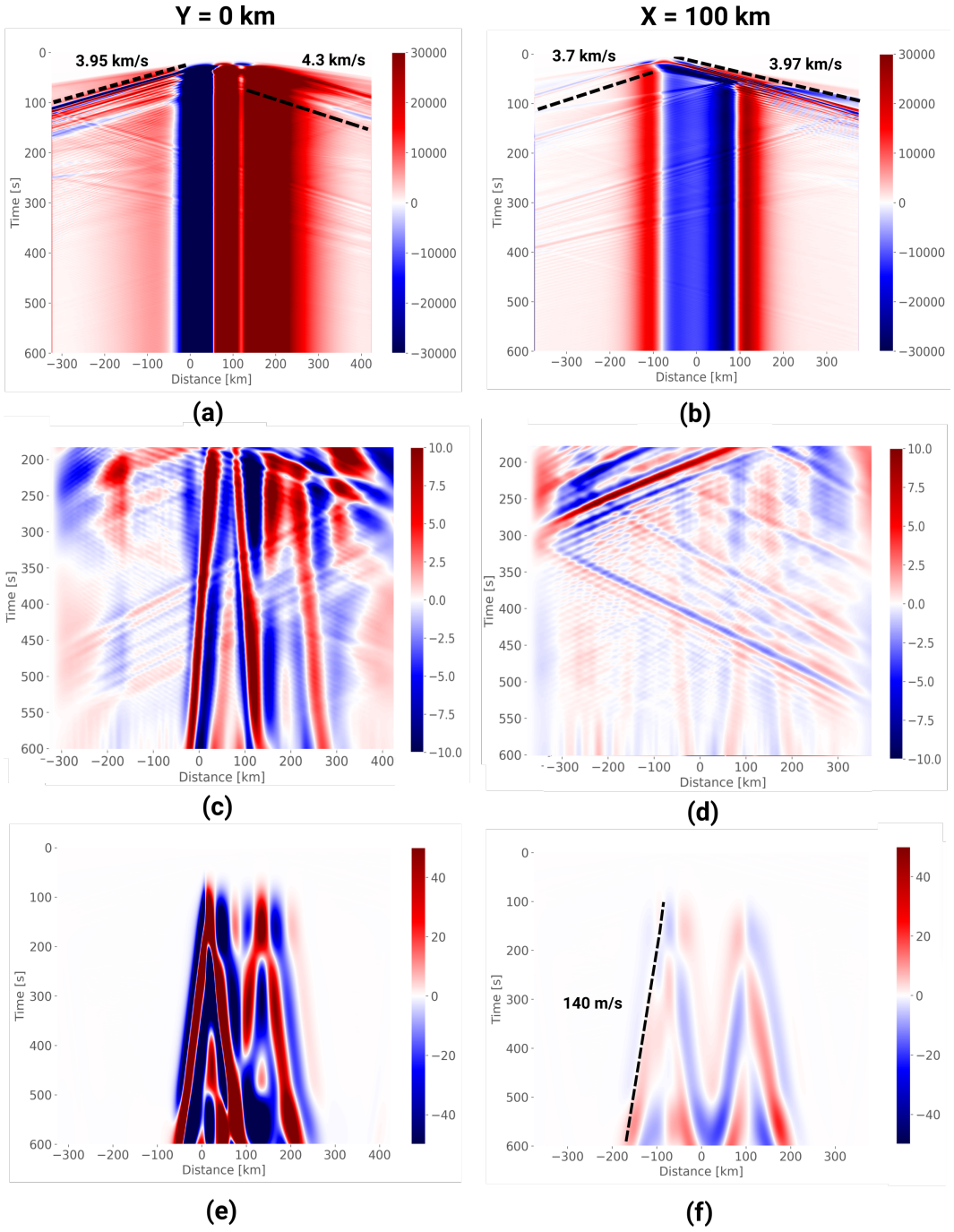

Figure 7. Strain signal corresponding to a trench-parallel array located at $y = 0$ km (left column) and a trench-orthogonal array at $x = 100$ km (right column). Top (a, b): Broadband strain recorded on seafloor-coupled receivers. Dashed black lines indicate seismic and surface wave velocities. Middle (c, d): same after removing the initial 180 secs, subtracting the mean of the final 180 secs (static seafloor deformation) from each receiver and F-K filtering seismic surface waves by bandpass filtering between 3 - 10 mHz onto the range of wavelengths (11 - 66 km) corresponding to propagating velocities between 110 - 200 m/s. Bottom (e, f): Estimated strain signal due to seafloor pressure (seafloor compliance and the cable's Poisson effect), derived by subtracting the vertical seafloor displacement from the sea surface height anomalies (SSHA, recorded by receivers near the top of the water column), F-K filtered as in (c, d). Strain is expressed as a signal-to-noise ratio (SNR) relative to the mean noise floor of the DAS instrument shown in Figure 2. The dashed black line in (d) indicates the tsunami phase velocity.

at shallow depth smoothly stops the rupture as it approaches the surface. The earthquake magnitude is $M_W = 8.5$ and the rupture propagates at 3.5 km/s on average.

Simulation outputs were recorded on 42000 receivers, slightly buried below the seafloor. Each receiver records velocity and stress at a 100 Hz sampling rate. They are arranged by pairs, with an intra-pair separation of 50 m, comparable to a commonly used DAS gauge length, and an inter-pair separation of 500 m. The receivers are arranged in 7 linear arrays, either parallel or orthogonal to the trench (Figure 6). The trench-parallel and trench-normal linear arrays, across and in the vicinity of the earthquake source area, represent end-member configurations of a seafloor cable.

Based on our previous analysis, we focus on longitudinal seafloor strain induced by the tsunami wave only from hydrostatic pressure, namely the compliance and Poisson effects (equations 6 and 7, respectively). We calculate the seafloor strain taking the finite difference between pairs of seafloor receivers as $\epsilon = \frac{u_1 - u_2}{d}$, where u_i is the displacement component parallel to the direction of the linear array at receiver i, and $d = 50$ m is the intra-pair receiver distance. The displacement is obtained by time integration of the velocity data.

To record SSHA, an additional set of receivers was placed near the top of the water column, directly above the seafloor receivers. We extract the SSHA from the vertical displacement of these receivers. Seafloor pressure is calculated from equation 10 based on the effective water column height, obtained by subtracting vertical seafloor displacement from SSHA. We then compute the estimated strain signal due to seafloor compliance and the cable's Poisson effect by using equations 6 and 7.

7.2 Enhancing the Tsunami Signal

The resulting seafloor strain fields for two profiles, one perpendicular to the fault ($y = 0$ km) and the other along the buried tip of the fault ($x = 100$ km), are shown in Figure 7 (a) and (b), respectively. The strain field is largely dominated by seismic and acoustic waves while the rupture propagates across the fault for ~ 60 s. The strain field continues to change after this time until it reaches final values at $t \sim 80$ s (Madden et al., 2021). From then on, the seafloor strain is dominated by the static deformation above and around the rupture area. Static displacements reach ~ 3 m along the $y = 0$ km line and 30 cm along the $x = 100$ km line.

The simulation data also contains spurious reflections originating from the boundaries of the computational domain. Thanks to the (non-perfect) absorbing boundary conditions, the amplitudes of these reflections are very small compared to the physical seismo-acoustic waves. However, they are large compared to the predicted tsunami-induced strain signals. These artifacts could be reduced with a simulation over a larger domain at higher computational cost or by employing more advanced boundary conditions, which is a non-trivial problem (e.g., Duru et al. (2019)).

Through data processing, we managed to visualize the tsunami signal in the simulation results. The simulated tsunami has a dominant wavelength of ≈ 57 km, which is much larger than the water depth. Thus, the shallow-water tsunami regime holds and we should be looking for tsunami signals propagating at speed $v \approx \sqrt{gh} = 140$ m/s. Within the initial 10 minutes simulated here, as the tsunami only propagates within the vicinity of the tsunamigenic region, detection requires techniques to discern the tsunami signals which can be orders of magnitude below the seismo-acoustic wave and static deformation signals. As exemplified in the raw broadband seafloor strain (Figure 7a,b), the tsunami signal is not readily visible, but becomes observable after the initial 180 seconds thanks to post-processing (Figure 7c,d). We first subtract on each channel an estimate of the static strain, the mean over the final 180 seconds. We then apply a window taper. We finally apply a frequency-wavenumber (F-K) filter in the frequency range of 3

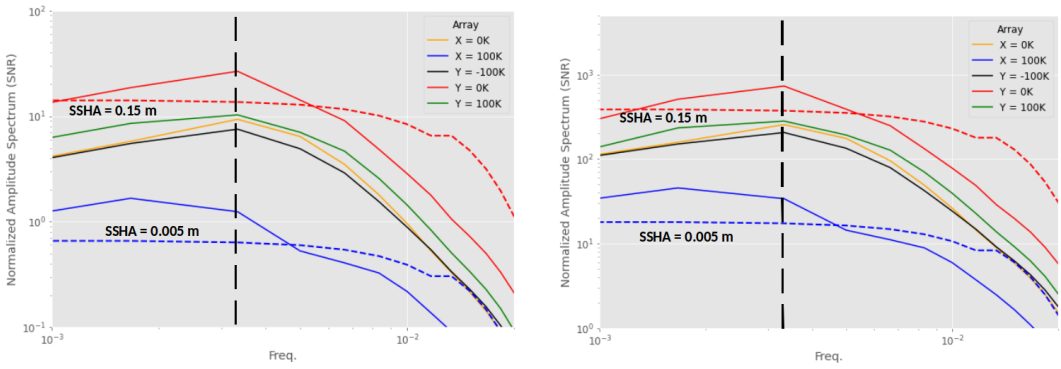

Figure 8. Amplitude Spectral Density (ASD) of the synthetic tsunami signal from the simulation due to (a) seafloor compliance and (b) the full hydrostatic pressure (Poisson and seafloor compliance). Pressure is derived from the effective vertical displacement, by subtracting the vertical displacement at the seafloor from the SSHA (receivers just below the sea surface). The PSD is calculated for each receiver and then averaged along each array. Power is converted to amplitude. The signal is normalized relative to instrument noise (SNR). Red and blue dashed lines follow the color assignment on the legend, where the labeled SSHA values correspond to the maximum displacement (after F-K filtering) observed on the given array. Such SSHA is used in equations 5 and 7 to define the predicted signal from the derived model. The dashed black line marks the dominant tsunami wave frequency.

- 10 mHz and wavelength range of 11 - 66 km. The wavelength range is derived from the frequency range by dividing by a range of wave velocities around the expected tsunami speed, namely 110 - 200 m/s. For the $y = 0$ km array, it was necessary to remove a single receiver in the vicinity of the trench which showed a spatially abrupt change in displacement polarity. Upon post-processing, we readily observe the tsunami wavefronts on the trench-parallel array (Figure 7c) and faintly on the trench-orthogonal array (Figure 7d). The seismo-acoustic and static signals that dominate the broadband seafloor strains (Figure 7a,b) are about three orders of magnitude larger than the tsunami strain signals (Figure 7e,f). Making abstraction of the spurious reflections from the simulation boundaries, this analysis confirms the presence of the tsunami signal in the simulated seafloor strain data.

Real-time data processing, which is a key requirement for TEWS, could entail working with strain rate instead of strain. An example of this approach is included in the supplementary materials. After applying the same F-K filtering we remove the static signal. However, the boundary reflections from the simulation remain strong, which obfuscates the tsunami phase in this simulation.

7.3 Comparison to DAS Sensitivity and to Theoretical Model

We compute the expected DAS SNR by taking the ratio between the filtered strain and the mean noise floor of the DAS instrument shown in Figure 2. Because this simulation did not model a seafloor cable, the contribution from Poisson's effect is not included in the simulation data shown in Figure 7c,d. But both seafloor compliance and Poisson's effect are included in Figure 7e,f, which is derived from the water column height simulation data. The SNR reaches values higher than 10 during the whole time window

along the trench-parallel array (Figure 7-c) and of order 1 along the trench-orthogonal array (Figure 7d).

Among the DAS array configurations examined here, we find that the best suited for tsunami detection is located close to the source area and perpendicular to the trench. We compare the simulated seafloor compliance signals over all receiver arrays, to the strain predicted by the theoretical model. We calculate the power spectral density of the estimated strain due to seafloor compliance at each receiver, based on their SSHA and vertical seafloor displacement, then average along each array, and take the square root to convert power to amplitude. The results are shown in Figure 8(a). The arrays at $y = \pm 200$ km are ignored because the tsunami does not reach them during the 10 minutes of simulation. The expected tsunami signal from the full hydrostatic effect (Poisson effect and seafloor compliance) is shown in Figure 8(b). The strongest signal is recorded on the $y = 0$ km array, which is aligned with the prevalent propagation direction of the tsunami. Overall, the theory gives an adequate order-of-magnitude estimate of the signal across all arrays. The two dashed curves in Figure 8 are the estimated signal for two selected values of SSHA (see labels), corresponding to the maximum SSHA for the array with the largest SSHA ($y = 0$ km) and for the array with the lowest SSHA ($x = 100$ km). The theoretical and the simulation amplitudes agree in order of magnitude. Their differences are attributable to the simplifying assumptions in the theoretical estimate: the same SSHA value at all frequencies, a single tsunami propagation direction.

8 Conclusion

Motivated by the need to advance tsunami warning systems and the fundamental understanding of tsunami processes, we have evaluated, through theoretical analysis and numerical simulations, the potential of Distributed Acoustic Sensing on seafloor fiber optic cables for direct observation of tsunami waves.

We derived first-order estimates of the seafloor DAS signals potentially generated by tsunamis. We considered two mechanisms through which the hydrostatic pressure perturbation of tsunami waves can induce longitudinal strain on a cable: the elastic deformation of the seafloor (compliance) and the Poisson effect within the cable. We also quantified two mechanisms by which the sub-horizontal deep water flow, induced by tsunami waves, can generate DAS signals: seafloor shear and temperature advection. However, we found them to have a relatively minor potential contribution in deep waters. Seafloor shear contributes significantly only at shallow depths (< 100 m) and for relatively large initial SSHA (> 0.1 m). The presence and amplitude of background temperature fluctuations can be assessed a priori and, if problematic, they can be selectively filtered out based on their slow propagation speed.
If the seafloor compliance and the Poisson effect on the cable represent the primary mechanisms through which DAS systems are anticipated to record the passage of tsunami waves; in order to achieve a sensitivity similar to that of a DART station (1 mm amplitude at 4 km water depth) (Mungov et al., 2013), the minimum amplitude of the strain signal to be resolved is $\epsilon \approx 5 \times 10^{-10}$ at frequencies in the order of tens of mHz. The current values of single-channel strain noise ASD of conventional DAS equipment operating at kHz sampling frequencies suggest that these water column changes will not be easily resolved without using the information from the full array. However, beamforming methods allowing fairly large processing gains, may probably lead to enough sensitivity, as shown in recent related efforts (Xiao et al., 2024). The strain noise ASD of conventional DAS systems in this frequency range is dominated by 1/f noise caused by reference updates and laser frequency drifts. Methods for improving the sensitivity of DAS instrumentation at these frequencies, such as the multi-frequency calibration technique (Vidal-Moreno et al., 2022), together with laser frequency stabilization, have already demonstrated a way to strongly mitigate this noise component and reach the low-frequency performance necessary for tsunami detection at almost single-channel level.

To further evaluate the use of DAS for TEWS, we carried out a full-physics simulation representative of a large earthquake rupture in a subduction zone. This simulation allowed to assess our ability to separate the tsunami contribution from the static and dynamic earthquake components, depending on their relative distance and the orientation of the cable. We found that the preferred cable orientation is aligned with the horizontal displacement most likely to occur (i.e. perpendicular to the trench), as the tsunami energy and propagation will mirror such a pattern and because DAS records longitudinal strain. While less optimal, cables perpendicular to the horizontal displacement are still relevant for tsunami detection. To optimize early warning times, it is best to detect the tsunami in the generating region, but cables directly over the subducting slab will also record the quasi-static seafloor displacement. The latter is orders of magnitude larger than the former and both have similar spatio-temporal characteristics. We show that it is still possible to retrieve the tsunami signal after appropriate filtering and after a few minutes of signal propagation. Furthermore, as seismo-acoustic waves can induce seafloor strains exceeding the maximum strain variation limit of the instrument, $\Delta\epsilon_{max} \approx \pm 82.5 \times 10^{-6}$, these signals will momentarily saturate the instrument. This would delay the tsunami detection by a few minutes (3 minutes in our simulation), but this delay remains compatible with the design of local TEWS as tsunami waves usually take more than 10-15 minutes to reach the nearby coasts. Possible strategies to reduce this delay may consist of customized signal processing, monitoring for the tsunami signal from strategically selected segments of the array, away from the strongest seismic signals, or by selecting a different array placement altogether.

The signal strength derived in the simulation can be considered a conservative estimate as the model consisted of a rigid solid earth model, representative of the oceanic crust. A more compliant seafloor due to the presence of sediments and less rigid layers near the surface amplifies low-velocity strain signals. This signal can be optimized by the degree of mechanical ground–cable coupling; this is especially the case when monitoring the compliance of low-confined upper layers containing large amounts of soft soils. Further enhancement can be attained by utilizing more compliant cables.

In summary, the theoretical and numerical considerations presented in this work point to the real possibility of detecting tsunami waves via fiber optic cable. With the vast existing network of submarine telecom cables, DAS provides an unprecedented opportunity to monitor and anticipate tsunamis. The advantages of DAS over other existing tsunami observation technologies include relatively low maintenance costs, wide and dense coverage, proximity to tsunamigenic sources (earthquakes or other), data availability in real time. With ongoing improvements in sensitivity at low frequencies, DAS could soon be poised as a key technology to enhance regional TEWS and to advance our understanding of tsunami processes.

Open Research Section

The synthetic dataset described in section 7 and accompanying Python routine to process and generate Figure 7; as well as Python routine to simulate the strain model outlined in sections 3 through 5 and generate Figures 4 and 5 is accessible via (Becerril, 2024) hosted by Recherche Data Gouv.

Acknowledgments

This work was supported by the European Innovation Council under Grant SAFE (ref. 101098992), the European Research Council (OCEAN-DAS: ERC-2019-POC-875302), the SEAFOOD project, funded by grant ANR-17-CE04-0007 of the French Agence Nationale de la Recherche and the Doeblin Federation (FR2800 CNRS). We thank Eric Dunham for providing results of a 2D fully-coupled simulation at an early stage of this work. AAG and FK acknowledge additional support from the European Union's Horizon 2020

research and innovation programme (TEAR ERC Starting; grant no. 852992) and Horizon Europe (ChEESE-2P, grant no. 101093038; DT-GEO, grant no. 101058129; and Geo-INQUIRE, grant no. 101058518) and from the National Science Foundation (MTMOD, grant no. EAR-2121666, LCCF-CSA, grant no. OAC-2139536, CRESCENT, grant no. EAR-2225286, Quakeworx grant no. OAC-2311208) and the National Aeronautics and Space Administration (grant no. 80NSSC20K0495). AAG and FK acknowledge the Gauss Centre for Supercomputing e.V. (www.gauss-centre.eu, projects pr63qo, pn49ha) for funding this project by providing computing time on the GCS Supercomputer SuperMUC-NG at Leibniz Supercomputing Centre (www.lrz.de).

References

Aoi, S., Asano, Y., Kunugi, T., Kimura, T., Uehira, K., Takahashi, N., ... Fujiwara, H. (2020). Mowlas: Nied observation network for earthquake, tsunami and volcano. *Earth, Planets and Space*, *72*, 126. doi: 10.1186/s40623-020-01250-x

Arai, K., Naruse, H., Miura, S., Kawamura, K., Hino, R., Ito, Y., ... Kasaya, T. (2013). Tsunami-generated turbidity current of the 2011 tohoku-oki earthquake. *Geology*, *41*, 1195–1198. doi: 10.1130/G34777.1

Becerril, C. (2024). *Replication Data for: Towards tsunami early-warning with Distributed Acoustic Sensing: expected seafloor strains induced by tsunamis* [Dataset]. Recherche Data Gouv. Retrieved from `https://doi.org/10.57745/ENBAIS` (Software routines also available) doi: 10.57745/ENBAIS

Bernard, E., & Titov, V. (2015). Evolution of tsunami warning systems and products. *Philosophical Transactions of the Royal Society A*, *373*, 20140371. doi: 10.1098/rsta.2014.0371

Bhatta, H. D., Costa, L., Garcia-Ruiz, A., Fernandez-Ruiz, M. R., Martins, H. F., Tur, M., & Gonzalez-Herraez, M. (2019). Dynamic measurements of 1000 microstrains using chirped-pulse phase-sensitive optical time-domain reflectometry. *Journal of Lightwave Technology*, *37*(18), 4888–4895.

Brenne, J. K., Sladen, A., Pecci, P., Morten, J. P., Pelaez, J., Jacobsen, J., ... Février, H. (2024). Non-intrusive das coexisting in telecom networks. In *Ofc conference san diego, 2024* (Vol. 2024).

Budiansky, B., Drucker, D., Kino, G., & Rice, J. (1979). Pressure sensitivity of a clad optical fiber. *Applied optics*, *18*(24), 4085–4088.

Crawford, W. (2004). The sensitivity of seafloor compliance measurements to subbasalt sediments. *Geophysical Journal International*, *157*, 1130–1145. doi: 10.1111/j.1365-246X.2004.02264.x

Dean, R. G., & Dalrymple, R. A. (1991). *Water wave mechanics for engineers and scientists* (Vol. 2). world scientific publishing company.

Diaz-Meza, S., Jousset, P., Currenti, G., Wollin, C., Krawczyk, C., Clarke, A., & Chalari, A. (2023). On the comparison of records from standard and engineered fiber optic cables at etna volcano (italy). *Sensors*, *23*(7), 3735.

Duru, K., Gabriel, A.-A., & Kreiss, G. (2019). On energy stable discontinuous galerkin spectral element approximations of the perfectly matched layer for the wave equation. *Computer Methods in Applied Mechanics and Engineering*, *350*, 898–937.

Dziewonski, A. M., & Anderson, D. L. (1981). Preliminary reference earth model. *Physics of the earth and planetary interiors*, *25*(4), 297–356.

Eble, M. C., González, F. I., Mattens, D. M., & Milburn, H. B. (1989). *Instrumentation, field operations, and data processing for pmel deep ocean bottom pressure measurements* (Tech. Rep.). N/A: NOAA Technical Memorandum ERL PMEL-89.

Fernandez-Ruiz, M. R., Martins, H., Costa, L., Martin-Lopez, S., & Gonzalez-Herraez, M. (2018). Steady-sensitivity distributed acoustic sensors. *J. Lightwave Technol.*, *36*, 5690–5696. doi: 10.1109/JLT.2018.2877849

Fernandez-Ruiz, M. R., Martins, H., Williams, E., Becerril, C., Magalhaes, R., Costa, L., ... Gonzalez-Herraez, M. (2022). Seismic monitoring with distributed acoustic sensing from the near-surface to the deep oceans. *J. Lightwave Technol.*, *40*, 1453–1463. doi: 10.1109/JLT.2021.3128138

Glover, H., Wengrove, M., & Holman, R. (2024). Measuring hydrodynamics and exploring nearshore processes using distributed sensing of fiber-optic cable strain. *Coastal Engineering*, 104487.

Guerin, G., Rivet, D., van den Ende, M. P., Stutzmann, E., Sladen, A., & Ampuero, J. P. (2022). Quantifying microseismic noise generation from coastal reflection of gravity waves recorded by seafloor das. *Geophysical Journal International*, *231*(1), 394–407.

Haavik, K. E. (2022). On the use of low-frequency distributed acoustic sensing data for in-well monitoring and well integrity: Qualitative interpretation. *SPE Journal*, 1–16. doi: 10.2118/212868-PA

Harris, R. A., Barall, M., Aagaard, B., Ma, S., Roten, D., Olsen, K., ... Ampuero, J. (2018). A suite of exercises for verifying dynamic earthquake rupture codes. *Seismological Research Letters*, *89*(3), 1146–1162.

Hartog, A., Conduit, A., & Payne, D. (1979). Variation of pulse delay with stress and temperature in jacketed and unjacketed optical fibres. *Optical and Quantum Electronics*, *11*, 265–273. doi: 10.1007/BF00620112

Heidarzadeh, M., & Gusman, A. (2019). Application of dense offshore tsunami observations from ocean bottom pressure gauges (obpgs) for tsunami research and early warnings. In T. Durrani, W. Wang, & S. Forbes (Eds.), *Geological disaster monitoring based on sensor networks* (pp. 7–22). Springer Singapore. doi: 10.1007/978-981-13-0992-2_2

Heinecke, A., Breuer, A., Rettenberger, S., Bader, M., Gabriel, A.-A., Pelties, C., ... Smelyanskiy, M. (2014). Petascale high order dynamic rupture earthquake simulations on heterogeneous supercomputers. In *Sc'14: Proceedings of the international conference for high performance computing, networking, storage and analysis* (pp. 3–14).

Ide, S., Araki, E., & Matsumoto, H. (2021). Very broadband strain-rate measurements along a submarine fiber-optic cable off cape muroto, nankai subduction zone, japan. *Earth, Planets and Space*, *73*(1), 1–10.

Inazu, D., & Hino, R. (2011). Temperature correction and usefulness of ocean bottom pressure data from cabled seafloor observatories around japan for analyses of tsunamis, ocean tides, and low-frequency geophysical phenomena. *Earth, planets and space*, *63*(11), 1133–1149.

Inazu, D., Ito, Y., Hino, R., & Tanikawa, W. (2023). Abrupt water temperature increases near seafloor during the 2011 tohoku earthquake. *Progress in Earth and Planetary Science*, *10*(1), 24.

Joseph, A. (2011). *Tsunamis: Detection, monitoring, and early-warning technologies.* Oxford: Academic Press.

Katsumata, A., Tanaka, M., & Nishimiya, T. (2021). Rapid estimation of tsunami earthquake magnitudes at local distance. *Earth Planets Space*, *73*, 72. doi: 10.1186/s40623-021-01391-7

Kohler, M. D., Bowden, D. C., Ampuero, J.-P., & Shi, J. (2020). Globally scattered 2011 tohoku tsunami waves from a seafloor sensor array in the northeast pacific ocean. *Journal of Geophysical Research: Solid Earth*, *125*(11), e2020JB020221. doi: https://doi.org/10.1029/2020JB020221

Kojima, N., Yabuta, T., Negishi, Y., Iwabuchi, K., Kawata, O., Yamashita, K., & Miyajima, Y. (1982). Submarine optical fiber cable: development and laying results. *Appl. Opt.*, *21*, 815. doi: 10.1364/AO.21.000815

Krenz, L., Uphoff, C., Ulrich, T., Gabriel, A.-A., Abrahams, L., Dunham, E., & Bader, M. (2021). 3d acoustic-elastic coupling with gravity: the dynamics of the 2018 palu, sulawesi earthquake and tsunami. In *Proceedings of the inter-*

national conference for high performance computing, networking, storage and analysis (pp. 1–14). doi: 10.1145/3458817.3476173

Lindsey, N. J., Dawe, T. C., & Ajo-Franklin, J. B. (2019). Illuminating seafloor faults and ocean dynamics with dark fiber distributed acoustic sensing. *Science*, *366*(6469), 1103–1107.

Lindsey, N. J., & Martin, E. R. (2021). Fiber-optic seismology. *Annual Review of Earth and Planetary Sciences*, *49*, 309–336.

Lior, I., Sladen, A., Rivet, D., Ampuero, J.-P., Hello, Y. M., Becerril, C., ... Markou, C. (2020). On the detection capabilities of underwater das (preprint). *Geophysics*. doi: 10.1002/essoar.10504330.1

Lotto, G. C., & Dunham, E. M. (2015). High-order finite difference modeling of tsunami generation in a compressible ocean from offshore earthquakes. *Computational Geosciences*, *19*(2), 327–340.

Madden, E. H., Bader, M., Behrens, J., van Dinther, Y., Gabriel, A.-A., Rannabauer, L., ... van Zelst, I. (2021). Linked 3-d modelling of megathrust earthquake-tsunami events: from subduction to tsunami run up. *Geophysical Journal International*, *224*(1), 487–516.

Maeda, T., Furumura, T., Sakai, S., & Shinohara, M. (2011). Significant tsunami observed at the ocean-bottom pressure gauges at 2011 off the pacific coast of tohoku earthquake. *Earth, Planets, and Space*, *63*, 803–808. doi: 10.5047/eps.2011.06.005

Masoudi, A., Belal, M., & Newson, T. (2013). A distributed optical fibre dynamic strain sensor based on phase-otdr. *Measurement Science and Technology*, *24*(8), 085204.

Meulé, S., Pelaez Quiñones, J. D., Bouchette, F., Sladen, A., Ponte, A. L., Maier, A., ... Coyle, P. (2024). Reconstruction of nearshore surface gravity waves from distributed acoustic sensing data. *ESS Open Archive*.

Mikada, H., Mitsuzawa, K., Matsumoto, H., Watanabe, T., Morita, S., Otsuka, R., & Sugioka, H. (2006). New discoveries in dynamics of an m8 earthquake-phenomena and their implications from the 2003 tokachi-oki earthquake using a long term monitoring cabled observatory. *Tectonophysics*, *426*, 95–105. doi: 10.1016/j.tecto.2006.02.021

Mungov, G., Eblé, M., & Bouchard, R. (2013). Dart® tsunameter retrospective and real-time data: A reflection on 10 years of processing in support of tsunami research and operations. *Pure and Applied Geophysics*, *170*, 1369–1384.

National Oceanic and Atmospheric Administration (NOAA) Pacific Marine Environmental Laboratory (PMEL) National Center for Tsunami Research (NCTR). (2023). *NOAA national data buoy center's DART program.* Retrieved from `https://nctr.pmel.noaa.gov/Dart/` (Retrieved from url-https://nctr.pmel.noaa.gov/Dart/)

Paitz, P., Edme, P., Gräff, D., Walter, F., Doetsch, J., Chalari, A., ... Fichtner, A. (2020). Empirical investigations of the instrument response for distributed acoustic sensing (das) across 17 octaves. *Bulletin of the Seismological Society of America*, *111*(1), 1–10. doi: 10.1785/0120200185

Pastor-Graells, J., Martins, H., Garcia-Ruiz, A., Martin-Lopez, S., & Gonzalez-Herraez, M. (2016). Single-shot distributed temperature and strain tracking using direct detection phase-sensitive otdr with chirped pulses. *Opt. Express*, *24*, 13121. doi: 10.1364/OE.24.013121

Pastor-Graells, J., Nuno, J., Fernandez-Ruiz, M., Garcia-Ruiz, A., Martins, H., Martin-Lopez, S., & Gonzalez-Herraez, M. (2017). Chirped-pulse phase-sensitive reflectometer assisted by first-order raman amplification. *J. Lightwave Technol.*, *35*, 4677–4683. doi: 10.1109/JLT.2017.2756558

Pelaez Quiñones, J. D., Sladen, A., Ponte, A., Lior, I., Ampuero, J.-P., Rivet, D., ... Coyle, P. (2023). High resolution seafloor thermometry for internal wave and upwelling monitoring using distributed acoustic sensing. *Scientific Reports*,

13(1), 17459.

Reid, J. A., & Mooney, W. D. (2023). Tsunami occurrence 1900–2020: A global review, with examples from indonesia. *Pure and Applied Geophysics*, *180*(5), 1549–1571.

R. Fernández-Ruiz, M., Costa, L., & F. Martins, H. (2019). Distributed acoustic sensing using chirped-pulse phase-sensitive otdr technology. *Sensors*, *19*, 4368. doi: 10.3390/s19204368

Saito, T. (2019). *Tsunami generation and propagation.* Springer Tokyo. doi: 10.1007/978-4-431-56850-6

Saito, T., Ito, Y., Inazu, D., & Hino, R. (2011). Tsunami source of the 2011 tohoku-oki earthquake, japan: Inversion analysis based on dispersive tsunami simulations. *Geophysical Research Letters*, *38*, L00G19. doi: 10.1029/2011GL049089

Sladen, A., Rivet, D., Ampuero, J., De Barros, L., Hello, Y., Calbris, G., & Lamare, P. (2019). Distributed sensing of earthquakes and ocean-solid earth interactions on seafloor telecom cables. *Nature Communications*, *10*, 5777. doi: 10.1038/s41467-019-13793-z

Steketee, J. (1958). On volterra's dislocations in a semi-infinite elastic medium. *Can. J. Phys.*, *36*, 192–205. doi: 10.1139/p58-024

Talley, L. D. (2011). *Descriptive physical oceanography: an introduction.* Academic press.

Tanaka, H., Tinh, N., & Sana, A. (2020). Transitional behavior of a flow regime in shoaling tsunami boundary layers. *JMSE*, *8*, 700. doi: 10.3390/jmse8090700

Tatekura, K., Yamamoto, H., & Ejiri, Y. (1982). Strain of optical fibres of an optical submarine cable on the sea bed. *Electron. Lett.*, *18*, 414. doi: 10.1049/el:19820284

Tinh, N., & Tanaka, H. (2019). Study on boundary layer development and bottom shear stress beneath a tsunami. *Coastal Engineering Journal*, *61*, 574–589. doi: 10.1080/21664250.2019.1672127

Titov, V., Song, Y., Tang, L., Bernard, E., Bar-Sever, Y., & Wei, Y. (2016). Consistent estimates of tsunami energy show promise for improved early warning. *Pure Appl. Geophys.*, *173*, 3863–3880. doi: 10.1007/s00024-016-1312-1

Titov, V. V., González, F. I., Bernard, E. N., Eble, M. C., Mojfeld, H. O., Newman, J. C., & Venturato, A. J. (2005). Real-time tsunami forecasting: Challenges and solutions. *Natural Hazards*, *35*, 35–41. doi: 10.1007/s11069-004-2403-3

Tsai, V., Ampuero, J.-P., Kanamori, H., & Stevenson, D. (2013). Estimating the effect of earth elasticity and variable water density on tsunami speeds: Elastic compressible tsunami speed. *Geophys. Res. Lett.*, *40*, 492–496. doi: 10.1002/grl.50147

Tsushima, H., Hino, R., Tanioka, Y., Imamura, F., & Fujimoto, H. (2012). Tsunami waveform inversion incorporating permanent seafloor deformation and its application to tsunami forecasting. *Journal of Geophysical Research: Solid Earth*, *117*(B3).

Ugalde, A., Becerril, C., Villaseñor, A., Ranero, C. R., Fernández-Ruiz, M. R., Martin-Lopez, S., ... Martins, H. F. (2022). Noise levels and signals observed on submarine fibers in the canary islands using das. *Seismological Society of America*, *93*(1), 351–363.

Uphoff, C., Rettenberger, S., Bader, M., Madden, E. H., Ulrich, T., Wollherr, S., & Gabriel, A.-A. (2017). Extreme scale multi-physics simulations of the tsunamigenic 2004 sumatra megathrust earthquake. In *Proceedings of the international conference for high performance computing, networking, storage and analysis* (pp. 1–16).

Vidal-Moreno, P., Rochat, E., Fermoso, P., Fernández-Ruiz, M., Martins, H., Martin-Lopez, S., ... Gonzalez-Herraez, M. (2022). Cancellation of reference update-induced 1/f noise in a chirped-pulse das. *Opt. Lett.*, *47*, 3588. doi: 10.1364/OL.465367

Waagaard, O. H., Rønnekleiv, E., Haukanes, A., Stabo-Eeg, F., Thingbø, D., Forbord, S., ... Brenne, J. K. (2021). Real-time low noise distributed acoustic sensing in 171 km low loss fiber. *OSA Continuum*, *4*, 688. doi: 10.1364/OSAC.408761

Ward, S. N. (2003). Tsunamis. In R. A. Meyers (Ed.), *Encyclopedia of physical science and technology (third edition)* (p. 175-191). Academic Press. Retrieved from `https://www.sciencedirect.com/science/article/pii/B0122274105007936` doi: 10.1016/B0-12-227410-5/00793-6

Watada, S. (2013). Tsunami speed variations in density-stratified compressible global oceans. *Geophysical Research Letters*, *40*(15), 4001–4006.

Wilcock, W., Schmidt, D., Vidale, J., Harrington, M., Bodin, P., Cram, G., & Delaney, J. (2016). Designing an offshore geophysical network in the pacific northwest for earthquake and tsunami early warning and hazard research. In *Oceans 2016 mts/ieee monterey* (pp. 1–8). doi: 10.1109/OCEANS.2016.7761291

Williams, E. F., Fernández-Ruiz, M. R., Magalhaes, R., Vanthillo, R., Zhan, Z., González-Herráez, M., & Martins, H. F. (2019). Distributed sensing of microseisms and teleseisms with submarine dark fibers. *Nature communications*, *10*(1), 5778.

Williams, E. F., Ugalde, A., Martins, H. F., Becerril, C. E., Callies, J., Claret, M., ... Zhan, Z. (2023). Fiber-optic observations of internal waves and tides. *Journal of Geophysical Research: Oceans*, *128*(9).

Xiao, H., Spica, Z. J., Li, J., & Zhan, Z. (2024). Detection of earthquake infragravity and tsunami waves with underwater distributed acoustic sensing. *Geophysical Research Letters*, *51*(2), e2023GL106767. doi: https://doi.org/10.1029/2023GL106767

Zhan, Z. (2020). Distributed acoustic sensing turns fiber-optic cables into sensitive seismic antennas. *Seismological Research Letters*, *91*, 1–15. doi: 10.1785/0220190112